Journal of Materials Science & Technology 110 (2022) 109–116

Contents lists available at ScienceDirect

Journal of Materials Science & Technology

journal homepage: www.elsevier.com/locate/jmst

Research Article

Ultrastrong and ductile BCC high-entropy alloys with low-density via dislocation regulation and nanoprecipitates

Xuehui Yan[a], Peter K. Liaw[b], Yong Zhang[a,*]

[a] Beijing Advanced Innovation Center of Materials Genome Engineering, State Key Laboratory for Advanced Metals and Materials, University of Science and Technology Beijing, Beijing 100083, China
[b] Department of Materials Science and Engineering, The University of Tennessee, Knoxville, TN 37996, United States of America

ARTICLE INFO

Article history:
Received 8 June 2021
Revised 14 July 2021
Accepted 1 August 2021
Available online 9 November 2021

Keywords:
High-entropy alloys
Mechanical properties
Dislocation
Nanoprecipitates
Strain hardening

ABSTRACT

The high strength is a typical advantage of body-centered-cubic high-entropy alloys (BCC–HEAs). However, brittleness and weak strain-hardening ability are still their Achilles' heel. Here, extraordinary strength together with good tensile ductility are achieved in $(Zr_{0.5}Ti_{0.35}Nb_{0.15})_{100-x}Al_x$ alloys (at.%, x = 10 and 20) at room temperature. Relatively low densities of less than 6 g/cm^3 are exhibited in these alloys. Designing nanoprecipitates and diversifying dislocation motions are the keys to achieving such salient breakthrough. It is worth noting that the tensile strength of 1.8 GPa in $(Zr_{0.5}Ti_{0.35}Nb_{0.15})_{80}Al_{20}$ alloy is a record-high value known in reported BCC–HEAs, as well as a tensile strain over 8%. Furthermore, the maximum strain of ~25% in $(Zr_{0.5}Ti_{0.35}Nb_{0.15})_{90}Al_{10}$ alloy can challenge existing limit value, and is accompanied with a tensile strength of 1.2 GPa. The current work does not only provide novel ultra-strong and tough structural materials with low density, but also sheds new light on designing BCC–HEAs with attractive performances and strain-hardening ability.

1. Introduction

Next-generation high-performance structural materials are required to possess ultrahigh strength, excellent ductility, as well as low-density design [1]. High-entropy alloys (HEAs), a kind of typical complex materials, have generated considerable excitement in the advanced structural materials due to its attractive comprehensive mechanical properties [2, 3]. The HEAs generally derive their properties not from a dominant component, but rather from multiple based elements, which provides possibility to explore desirable performances in a wide composition space. In most of studied HEAs, the alloys with face-centered-cubic (FCC) structures or "FCC-based" structure show excellent ductility, but generally accompanied with low yield strengths [4–6]. In comparison, the alloys dominated by body-centered-cubic (BCC) structures possess relatively-high intrinsic yield strengths [7,8]. Recently, many efforts have been made to develop novel ultra-strong structural materials based on the BCC–HEAs.

However, the tensile ductility of BCC–HEAs seems relatively conventional. Brittleness and short-term strain-hardening ability are their Achilles' heel [9–12]. Some BCC–HEAs with ultra-high strengths fail to be stretched, while others can undergo plastic deformation and generally have weak strain-hardening abilities, making materials unstable after yielding. Overall, the lattice mismatch of BCC–HEAs is larger than that of other HEAs [3]. In this case, BCC–HEAs have a significant local stress fluctuation effect, which is not conductive to the dislocation slip and leads to intrinsic brittleness. Many efforts have been devoted to obtaining tensile ductility in BCC alloys, including reducing the sample size, inducing phase metastability and decreasing valence electron number [13–15]. At present, limited alloy systems possess tensile ductility, such as TiZrHfNb, TiZrHfNbTa, and NbMoTaW, etc. [11, 13-15]. Developing ultra-strong BCC–HEAs with good ductility and effective strain-hardening is a key to making them potential structural materials in technological applications.

To date, the strengthening mechanisms of HEAs can be concluded into three aspects: (i) Intrinsic strengthening via concentrated solid solution structures [16–18]; (ii) Tailoring the stability of the constituent phases by designing transformation / twinning-induced ductility, and regulating the chemical short-order and nanoprecipitates [19–22]; (iii) Industrial thermo-mechanical treatments via severe deformation and subsequently heat treatments [23,24]. In fact, many efforts on strengthening mechanisms are focused on the FCC–HEAs [25,26]. It is still weak to regulate the

* Corresponding authors.
E-mail address: drzhangy@ustb.edu.cn (Y. Zhang).

https://doi.org/10.1016/j.jmst.2021.08.034
1005-0302/

plastic deformation behavior of BCC–HEAs via above mechanisms, especially breaking through tensile brittleness at room temperature.

Another intriguing issue here is that how to achieve effective strain hardening to further ensure the stable tensile deformation in BCC–HEAs? Remarkably, plastic deformation of BCC–HEAs also shows some unique characterizations [27–31]. Researches have proved that composition inhomogeneities in HEAs play a positive role on kink nucleation of screw dislocations [32–34], which means that the kink nucleation in BCC–HEAs is easier than traditional BCC alloys. In this case, the kink nucleation promoted by local composition fluctuations significantly increases the density of screw dislocations, which causes extra dislocation pinning effect and forms high-density cross-kinks in BCC–HEAs. Although the strength is improved, high-density cross-kinks are not benefit for uniform and stable plastic deformation, and thereby accelerating the appearance of stress concentration [35]. Hence, it is inferred that regulating dislocation mobility is the key to solving the brittleness and weak strain-hardening.

On this basis, this work has made efforts from two aspects: (i) inducing precipitation via composition control, and (ii) diversifying the dislocation modes by through thermomechanical processing. Here, we successfully develop BCC–HEAs in the composition of $(Zr_{0.5}Ti_{0.35}Nb_{0.15})_{100-x}Al_x$ (at.%, x = 10 and 20), which possess ultrahigh strengths and good tensile ductility. The design philosophy is to enhance comprehensive properties and strain-hardening abilities of brittle BCC–HEAs by designing nanoprecipitates and simultaneously diversifying dislocation motions. The $(Zr_{0.5}Ti_{0.35}Nb_{0.15})_{90}Al_{10}$ alloy is treated as a model composition to clarify the deformation mechanism and strain-hardening capability.

2. Material and methods

2.1. Processing

Alloy with nominal composition of $(Zr_{0.5}Ti_{0.35}Nb_{0.15})_{100-x}Al_x$ (at.%, x = 10 and 20), were prepared by arc-melting a mixture of the constituent elements with purity higher than 99.9% under a Ti-gettered argon atmosphere. For simplicity, the two BCC–HEAs, namely $(Zr_{0.5}Ti_{0.35}Nb_{0.15})_{100-x}Al_x$ (in at.%, x = 10 and 20) are referred to as Al10 and Al20, respectively. The alloy ingots were remelted at least five times to improve the compositional homogeneity, and eventually drop-cast into a copper mold with size of 10 mm (width) × 10 mm (thickness) × 80 mm (length). Two samples were produced through thermomechanical process based on as-cast $(Zr_{0.5}Ti_{0.35}Nb_{0.15})_{90}Al_{10}$ alloy. One was fabricated by cold-rolling as-cast ingot to a reduction of 50%, and then carried out a recovery annealing treatment for 30 min at 700 °C (referred to as “recovery Al10 alloy”). The other was fabricated by cold-rolling as-cast ingot to a reduction of 80%, and then subjected to a recrystallization treatment for 30 min at 750 °C (referred to as the “recrystallization Al10 alloy”). Both were followed by air-cooled.

2.2. Mechanical testing

Sheet tensile samples with a gage length of 46 mm and cross-section of 5 mm × 1.2 mm were cut and mechanically polished to 2000 grit size. Cylindrical compression samples with a dimeter of 2 mm and height of 4 mm were cut and mechanically polished to 2000 grit size. Room-temperature tension and compression tests were evaluated using a CMT4105 universal electronic tensile testing machine with an initial strain rate of 1.0×10^{-3} s^{-1}. For each alloy, at least three samples were conducted by tensile and compressive tests.

2.3. Microstructural characterization

Crystal structure of the alloy was conducted using X-ray diffraction (XRD, BRUKERD8 Discover) with Cu Kα radiation. The $\theta-2\theta$ scanning was conducted in the range of 20°−100° with a scanning speed of 4°/min. Morphologies were characterized by a Zeiss Supra55 filed emission scanning electron microscopy (SEM) equipped with electron back-scattering diffraction (EBSD) spectrometer. Microstructure of deformed specimens was characterized by a transmission electron microscope (TEM, Tecnai F30) operated at 300 kV. The chemical concentration of alloys was investigated using the local electrode atom probe tomography (APT, LEAP 5000 × SI), and the sharp APT tip was prepared by the conventional Focused Ion Beam (FIB, FEI Helios Nanolab 600i) milling process.

2.4. Processing method of strain hardening curve

The strain-hardening rate were calculated:

$$\theta = d\sigma_t/d\varepsilon_t \quad (1)$$

where ε_t and σ_t are true strain and true stress, calculated from the engineering strain (ε_E) and engineering stress (σ_E). The specific functional relationships are as follows:

$$\varepsilon_t = \ln(1+\varepsilon_E) \quad (2)$$

$$\sigma_t = \sigma_E \times (1+\varepsilon_E) \quad (3)$$

In fact, the original resultant curves are accompanied by obvious short-range noises. To better exhibit the strain-hardening behavior, the experimental curve was smoothed by fitting a high order polynomial (using Origin software) to remove the irregularities and fluctuations.

3. Results

3.1. Alloy design, structure, and chemical composition

It should be noted that the two $(Zr_{0.5}Ti_{0.35}Nb_{0.15})_{100-x}Al_x$ alloys are developed on the basis of the ternary $Zr_{0.5}Ti_{0.35}Nb_{0.15}$ alloy, which was designed by high-throughput screening utilizing the multi-target co-sputtering combined with physical masking (Fig. 1(a-I): Screening) and exhibited excellent comprehensive mechanical properties in our previous work [36, 37]. To inspire the dual effect of entropy and enthalpy, the Al element was added into the ternary $Zr_{0.5}Ti_{0.35}Nb_{0.15}$ alloy (Fig. 1(a-II): Regulation). According to the binary mixing enthalpy illustrated in Fig. 1(a), there are non-negative mixing enthalpies between Zr, Ti, and Nb, while the mixing enthalpies between the Al and other components are negative [38], which provides thermodynamic possibilities for designing nanostructures in BCC–HEAs. As indicated by XRD patterns, both Al10 and Al20 alloys possess a single BCC solid-solution structure (Fig. 1(a)). The specific nominal composition, actual composition, and theoretical densities of BCC–HEAs are presented in Table 1. Remarkably, the densities of the two alloys are relatively low, ranging from 5.0 to 5.8 g/cm^3.

Here, taking the as-cast Al10 alloy as an example, the morphology and crystal structure are discussed. The alloy was eventually drop cast into a rod with a rectangular cross-section. The EBSD map taken from the cross-section of the as-cast bar displays a typical casting structure (Fig. 1(b)), which contains both equiaxed and columnar grains with grain sizes ranging from tens of nanometers to 1000 μm. The TEM image and the corresponding selected area electron diffraction (SAED) pattern confirm no other crystalline phases in the BCC matrix (Fig. 1(c)), further demonstrating that the as-cast alloy has a single BCC solid-solution structure.

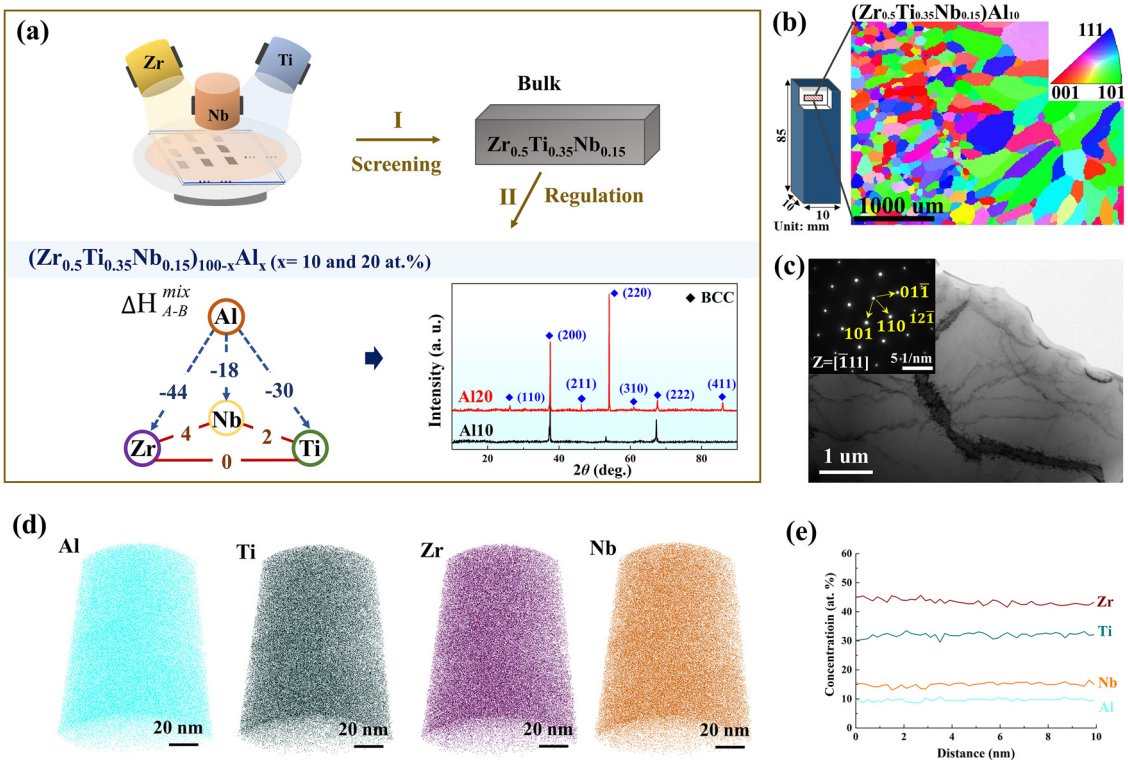

Fig. 1. Composition design and structure of $(Zr_{0.5}Ti_{0.35}Nb_{0.15})_{100-x}Al_x$ alloys. (a) Schematic diagram of composition-design philosophy. The internal XRD shows a single BCC lattice structure of as-cast $(Zr_{0.5}Ti_{0.35}Nb_{0.15})_{100-x}Al_x$ alloys. (b) EBSD maps of the $(Zr_{0.5}Ti_{0.35}Nb_{0.15})_{90}Al_{10}$ alloy. (c) TEM bright-field image of the as-cast $(Zr_{0.5}Ti_{0.35}Nb_{0.15})_{90}Al_{10}$ alloy. The corresponding selected area electron diffraction (SAED) pattern is as an inset. (d, e) 3D APT reconstructions: atomic distributions and concentration of components.

Table 1
Nominal composition, actual composition, and theoretical densities of the $(Zr_{0.5}Ti_{0.35}Nb_{0.15})_{100-x}Al_x$ alloy.

Nominal composition (at.%)	Actual composition (at.%)	Theoretical densities (g/cm^3)	Formula:
$(Zr_{0.5}Ti_{0.35}Nb_{0.15})_{90}Al_{10}$	$Zr_{45.9}Ti_{31.0}Nb_{12.7}Al_{10.4}$	5.79	$\rho=\frac{\sum C_i A_i}{\sum \frac{C_i A_i}{\rho_i}}$
$(Zr_{0.5}Ti_{0.35}Nb_{0.15})_{80}Al_{20}$	$Zr_{41.3}Ti_{27.8}Nb_{11.4}Al_{19.5}$	5.58	

Note: C_i, A_i, and ρ_i are the concentration, atomic weight, and density of i_{th} element, respectively.

To reveal chemical distribution at the atomic scale, 3D APT tests of tip specimens were taken from the Al10 alloy (Fig. 1(d)). Clearly, the distribution of all the elements is uniform. The component ratio is show in Fig. 1(e), which is consistent with the nominal composition.

3.2. Initial mechanical behaviors

The tensile and compressive testing of BCC–HEAs was carried out at room temperature. The compressive stress-strain curves exhibit ultrahigh tensile strength and outstanding plasticity of the two alloys, as presented in Fig. 2(a). The average yield strengths of Al10 and Al20 alloys are 978 MPa and 1368 MPa, respectively. No fracture is observed in Al10 and Al20 alloys with a compression deformation of up to 50%. The compressed morphologies of Al10 and Al20 specimens are illustrated as insets in Fig. 2(a), showing typical plastic deformation with a drum-shape.

The tensile stress-strain curves of $(Zr_{0.5}Ti_{0.35}Nb_{0.15})_{100-x}Al_x$ alloys are shown in Fig. 2(b). Even without any microstructural homogenization or optimization, Al10 alloy exhibits a fracture elongation of 14.3% together with a yield strength larger than 1000 MPa. Nevertheless, the as-cast Al20 alloy failed to be stretched due to casting defects. Here, a cold rolling process with a reduction of 50% was performed in alloys to eliminate casting defects. After cold-rolling, Al10 alloy exhibits a fracture elongation of ~9.2% together with a yield strength of 1143 MPa, and an ultimate tensile strength of 1286 MPa, as seen in Fig. 2(b). It is exciting to find that the tensile strength of the cold-rolled Al20 alloy is as high as 1803 MPa, and still maintain a tensile strain of 8.1%, which is a record-high strength known in BCC–HEAs. The specific values of the tensile test are illustrated in the inset of Fig. 2(b).

3.3. Mechanical behaviors after thermomechanical processing

Taking $(Zr_{0.5}Ti_{0.35}Nb_{0.15})_{90}Al_{10}$ alloy as a model composition, we next examine tensile properties of alloys with different microstructures, in order to further optimize the comprehensive properties and explore effective strain hardening mechanism (Fig. 3). Here, two samples were produced through controlled thermomechanical treatments. One is subjected to cold rolling and recovery annealing, referred to as the “recovery Al10 alloy”; The other is subjected to cold rolling and recrystallization annealing, referred as the “recrystallization Al10 alloy”.

The EBSD images of recovery and recrystallization Al10 alloys are indicated in the of Fig. 3(a) and (b), respectively. For the recovery Al10 alloy, the broken grains caused by cold rolling did not restored after short-term annealing. The orientation map in Fig. 3(a-I) proves that a relative low residual stress exists in the recovery alloy. In this case, it is desirable that some residual dislocations are reserved in the grain, which can be further confirmed by Fig. 3(a-II). In contrast, the complete recrystallization is performed in the

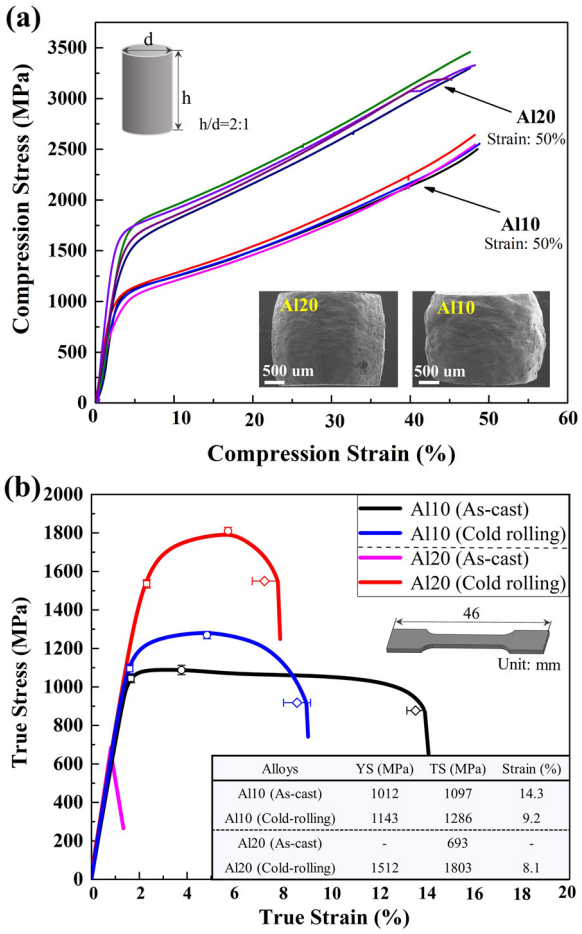

Fig. 2. Compressive and tensile properties of $(Zr_{0.5}Ti_{0.35}Nb_{0.15})_{100-x}Al_x$ alloys at room temperature. (a) Compressive engineering stress-strain curves. Morphologies of compressed Al10 and Al20 samples as insets. (b) The true tensile stress-strain curves of Al10 and Al20 alloys. (Abbreviation: yield strength (YS), tensile strength (TS), and tensile strain (ε)).

recrystallization Al10 alloy, with grain sizes ranging from several nanometers to 50 μm, as shown in Fig. 3(b).

The true stress-strain curves of recovery and recrystallized alloys are shown in Fig. 4(b). The recovery Al10 alloy show a significant improvement in the tensile strength of 1330 MPa with an acceptable ductility of 9.7%. It is exciting to conclude that the recrystallization alloy possesses a tensile strength of 1185 MPa and an outstanding ductility of 24.9%. Compared with the as-cast alloy, the tensile strength and strain of the recrystallization Al10 alloy are increased by ~8% and ~75%, respectively. The excellent ductility of ~25% in recrystallization Al10 alloy can challenge existing limit value of reported BCC alloys. Moreover, the strain-hardening ability of recovery and recrystallized alloys was significantly improved.

4. Discussion

4.1. Deformation mechanism of as-cast alloys

To clarify the deformation mechanism in the as-cast Al10 alloy, the deformed microstructures were analyzed from different tensile strains. The dislocation patterns are illustrated by Fig. 4(a), including the low strain (~1%) of a-I, medium strain (~3%) of a-II, and larger strain (~10%) of a-III. Three different tensile strains were sampled at the front, middle, and back of the tensile samples, which is corresponding to Fig. 4(b). As illustrated in Fig. 4(a-I), under slight deformation, one visible slip system of screw dislocations is observed in the form of straight dislocation lines parallel to each other. Certainly, there are already many curved edge dislocation lines. It indicates that the screw dislocations have nucleated and slipped in the early stage of deformation. Subsequently, the poly slip systems are activated as the deformation strain increases (Fig. 4(a-II)). Under high strain, the highly-concentrated dislocation-band structures, consisting of long and straight dislocation lines, are the typical sub-structure of dislocations. A grid structure is formed due to the interaction between dislocation bands, as demonstrated in Fig. 4(a-III).

The aggregation of dislocations in the dislocation bands inevitably cause dislocation tangles, accompanied with many dipoles and loops (Fig. 4(c)), which slows down the dislocation movement rate and has the possibility to cause stress concentration [39,40]. In this case, the occurrence of cross-slip contributes to the stability of plastic deformation. In addition to common cross-slip, double cross-slip is also observed (Fig. 4(d)), indicating good mobility of these long and straight dislocations. Frequent cross-slipping is helpful to the plastic deformation, but it is not beneficial to obtain effective strain hardening. Moreover, the microstructure of as-cast Al10 alloy is clearly heterogeneous with dislocations gathering

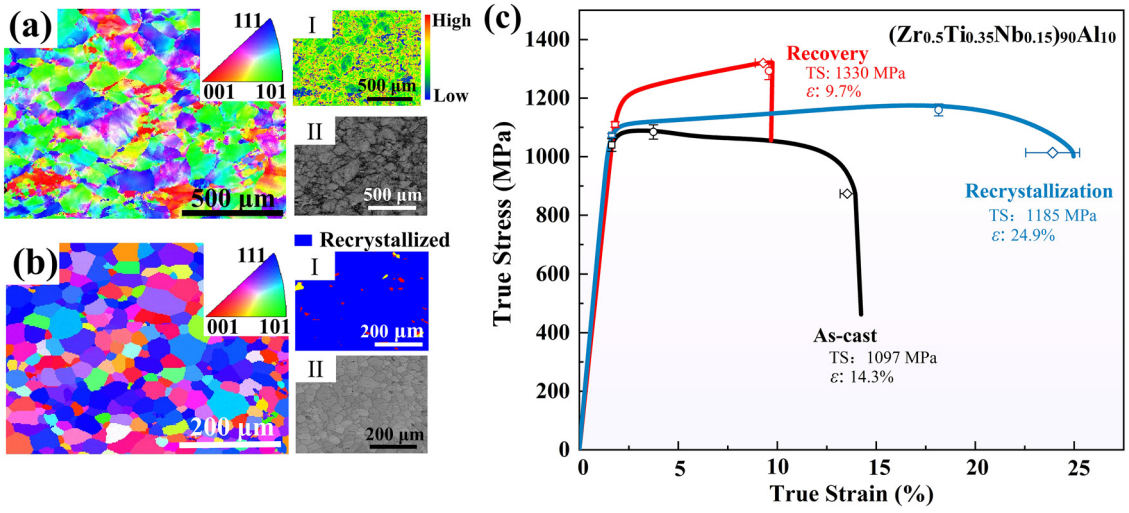

Fig. 3. Microstructure and tensile properties of recovery and recrystallization $(Zr_{0.5}Ti_{0.35}Nb_{0.15})_{90}Al_{10}$ alloys. (a) Microstructure of the recovery Al10 alloy (a-I: Orientation map, a-II: grain map). (b) Microstructure of the recrystallization Al10 alloy (b-I: recrystallization map, b-II: grain map). (c) The true tensile stress-strain curves.

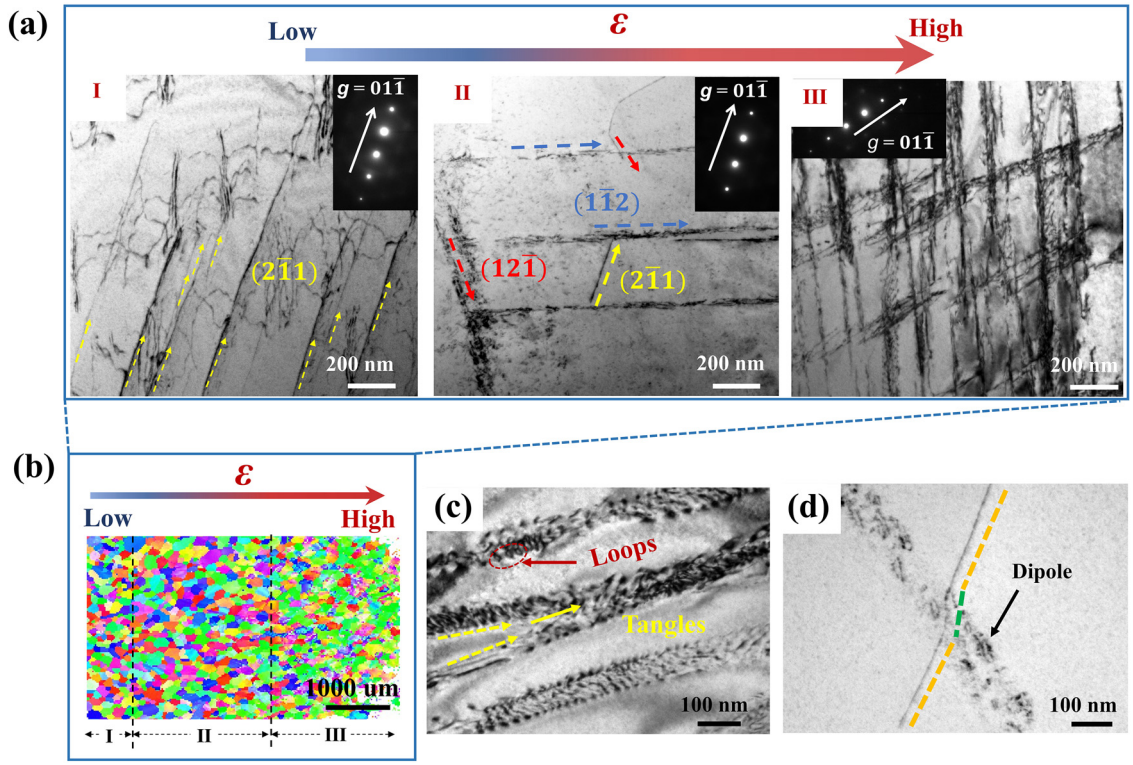

Fig. 4. Deformed microstructure of the as-cast Al10 alloy. (a) TEM observation of the dislocation pattern in different tensile strains (ε): low strain of a-I, middle strain of a-II, and high strain of a-III. (b) EBSD image of tensile fracture. The regions I, II, and III correspond to a-I, a-II, and a-III, respectively. (c) A magnified view of loops and dislocation tangles. (d) A magnified view of double dislocation cross-slip.

in dense bands, and some dislocation-free regions in-between the bands. Hence, it can be inferred that slowing down the frequency of cross-slip and homogenizing the deformation microstructure are the keys to obtain better ductility and strain hardening capacity.

4.2. Deformation mechanism of recovery and recrystallization alloys

Totally different deformation mechanisms were captured in the recovery and recrystallization Al10 alloys. Precipitates and different dislocation motion modes were obtained after thermo-mechanical treatments. For the recovery Al10 alloy, high-density dislocation cells are formed around the nanoprecipitates (Fig. 5(a)). As we discussed, the dislocations caused by cold rolling are partially retained in the recovery Al10 alloy after short-term annealing. During the plastic deformation, reserved dislocations significantly promote the dislocation tangling and pinning, and further form high-density dislocation cells. The interaction between the nanoprecipitates and high-density dislocation cells can improve deformation resistance and suppress ineffective strain hardening caused by cross-slip.

For the recrystallization Al10 alloy, precipitation strengthening is still the main mechanism for ultrahigh strength and ductility. As indicated in Fig. 5(b), unlike the dislocation cells in the recovery Al10 alloy, there are many short rod dislocations dispersed in the deformed grains. The magnified view of short-rod dislocations is exhibited in the inset picture. The appearance of short rod dislocations is attributed to the refined grains, which makes the deformation more uniform. Compared with the as-cast Al10 alloy, the deformation microstructure of recrystallization Al10 alloy is more homogeneous. The uniform and dense short-rod dislocations promote to obtain effective pinning and flexible interactions, which further ensure the excellent comprehensive mechanical properties and strain-hardening ability.

Magnified views provide the direct evidence of the interaction between precipitates and dislocation (Fig. 5(c)). In fact, both the shearing and Orowan bypass mechanisms occur in nanoprecipitates, which are two major mechanisms for precipitate strengthening [41]. In particular, the shearing mechanism is more active in some small-sized precipitations, while a pure bypass mechanism usually occurs in large-sized precipitates. The Fig. 5(d) exhibits the morphology and composition of nanoprecipitates, revealing that the spherical precipitate also contains multiple components. The element Zr and Al are concentrated in precipitates compared with matrix. The corresponding SAED pattern in Fig. 5(e) proves that these precipitates possess a BCC lattice structure. And the precipitate and matrix phase follow an orientation relationship of $(01\bar{1})_{matrix}$ // $(\bar{2}1\bar{1})_{precipitate}$ and $[011]_{matrix}$ // $[011]_{precipitate}$. The interplanar spacings of matrix and precipitates are 0.249 nm and 0.287 nm, respectively, as show in HRTEM image of Fig. 5(f). The misfit between matrix and precipitates is about 6.2%, indicating that it is a semi-coherent interface.

4.3. Analysis of strain-hardening ability

It is clearly observed that effective strain-hardening abilities are obtained in recovery and recrystallization Al10 alloys, as shown in Fig. 6(a). Unlike as-cast alloys that soften after yielding, the recovery alloy exhibits a high strain-hardening rate, while the strain hardening of the recrystallization alloy is stable and durable. Here, the nanoprecipitates and dislocation motion significantly affected the strain-hardening ability. The schematic diagrams of strain-hardening mechanisms are demonstrated in the inset of Fig. 6(a).

For the as-cast Al10 alloy, the plastic deformation is totally dominated by the dislocation glide, especially the long and straight dislocation. Heterogenous dislocation microstructure and frequent cross-slip result in weak strain hardening ability. The improvement in strain hardening capability is attributed to two key factors:

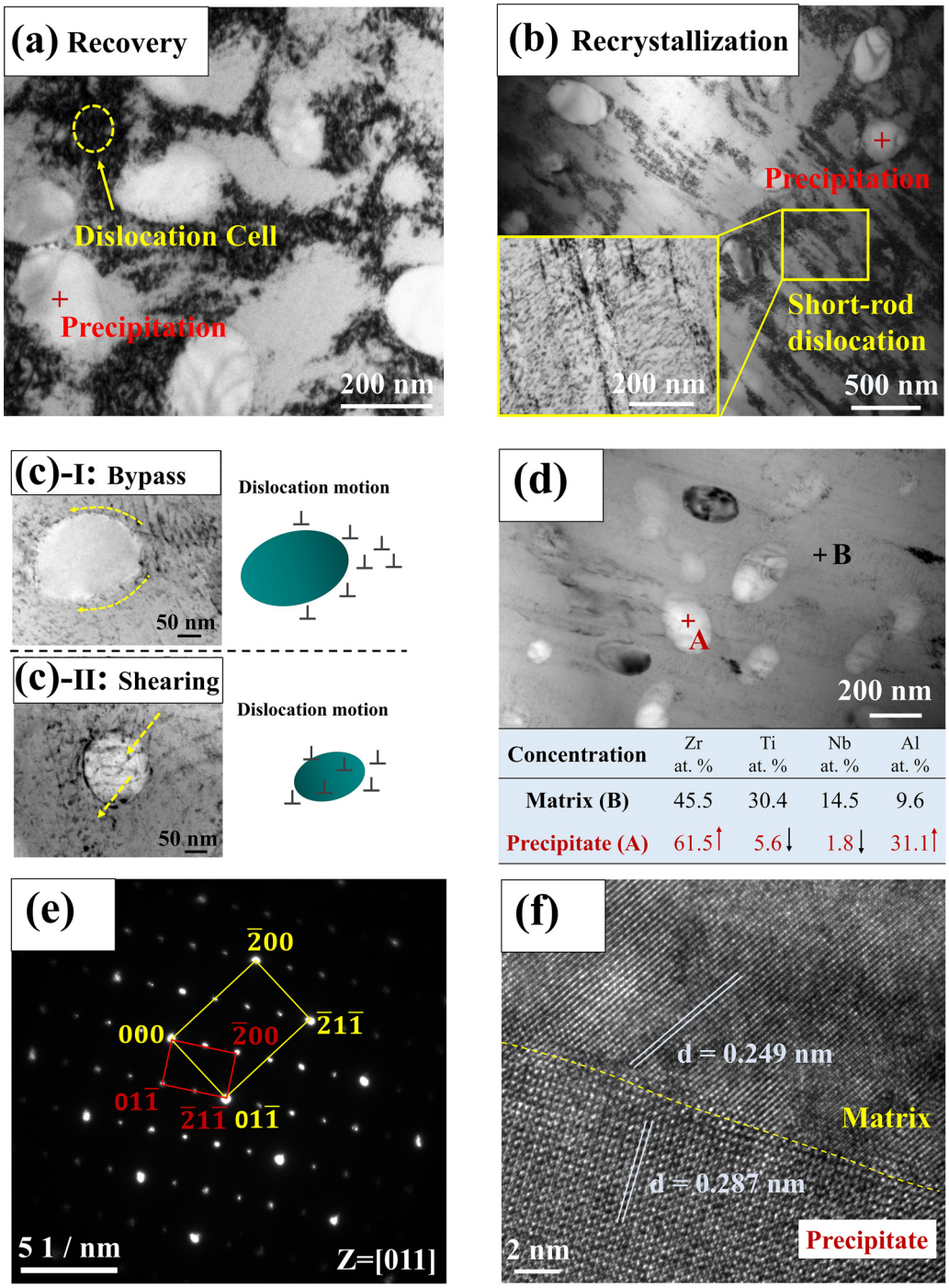

Fig. 5. Deformed microstructure of recovery and recrystallization Al10 alloys. (a, b) Deformation microstructure in recovery and recrystallization Al10 alloy. Magnified view of short-rod dislocations is as an inset in Fig. 5(b). (c) Morphology of the interaction between nanoprecipitates and dislocations: (c-I) dislocation bypass mechanism; (c-II) dislocation-shearing mechanism. (d) Morphology and composition of spherical precipitates. (e) SAED pattern of matrix and nanoprecipitates. Matrix and precipitates are highlighted in yellow and red, respectively. (f) HRTEM image of the matrix and nano-precipitates.

(i) Designing nanoprecipitates to obtain the significant interaction with dislocation; (ii) Diversifying dislocation motions to improve mobility and achieve homogeneous dislocation microstructure. For recovery Al10 alloys, the high-density dislocation cells formed by tangling between reserved dislocations and tensile dislocations contribute to achieve higher deformation resistance, thereby improving the strain hardening ability. Simultaneously, nanoprecipitates also play a positive role in the pinning of dislocations. Unlike the notable but short-live strain hardening effect in the recovery A10 alloy, the recrystallization Al10 alloy possesses a stable and durable strain-hardening ability. On the one hand, precipitates significantly increase local slip resistance, and slow down the dislocation motions. On the other hand, refined grains in recrystallization Al10 alloy make the deformation more uniform. Thus, a compact and homogeneous short-rod dislocation microstructure is obtained. In this case, the effective pinning and frequent interactions of dislocations are easily achieved, which plays a positive role on stable strain hardening and makes the alloy tougher and stronger simultaneously.

The essential factors of deformation are briefly illustrated in Fig. 6(b). The as-cast Al10 alloy is only dominated by dislocations, while recovery and recrystallization Al10 alloys are affected by nanoprecipitates and dislocations. For the recovery Al10 alloy, the key factors are concluded as dislocation cells and nanoprecipitates.

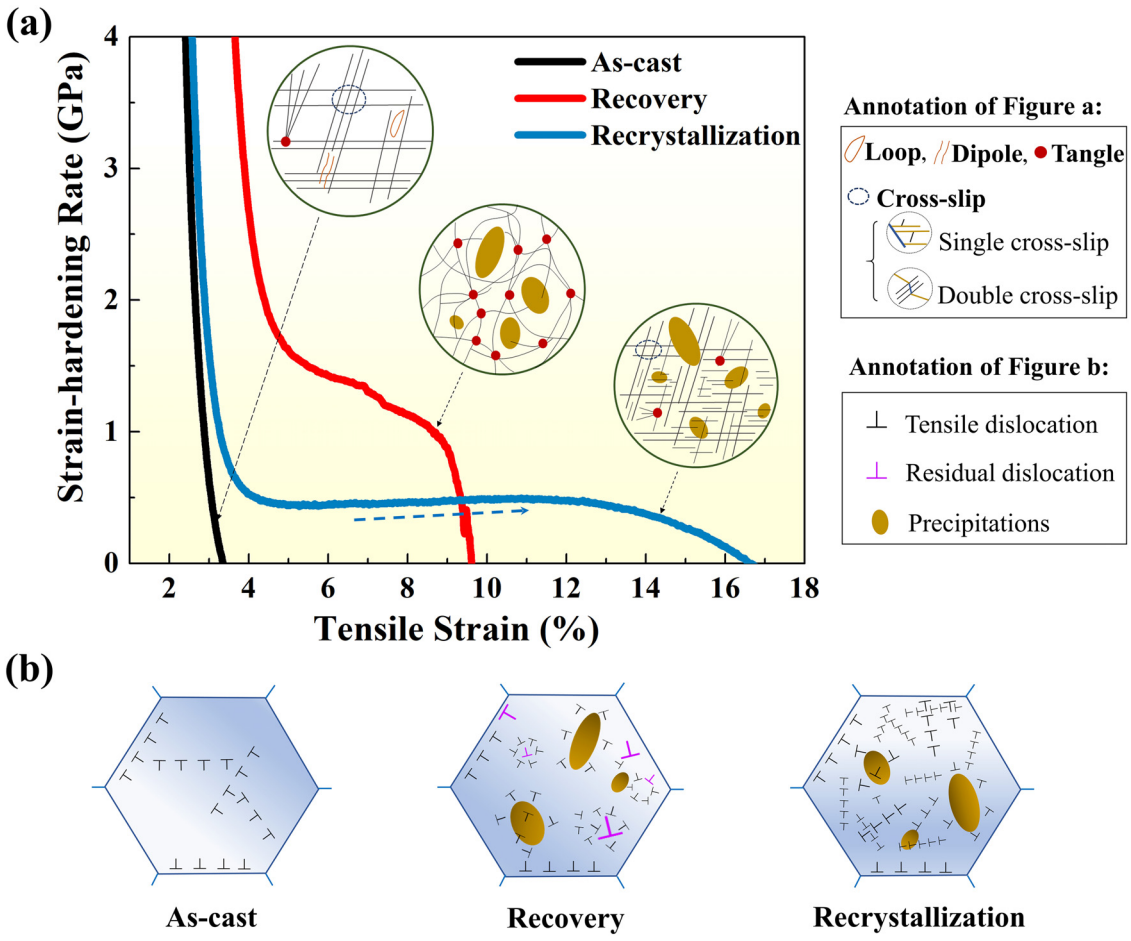

Fig. 6. Discussion of strain-hardening ability. (a) Strain-hardening ability and related microstructures. (b) Schematic illustration of deformation mechanisms. [Residual dislocations: reserved after cold-rolling and recovery annealing. (Tensile dislocations: generated during the tensile deformation).

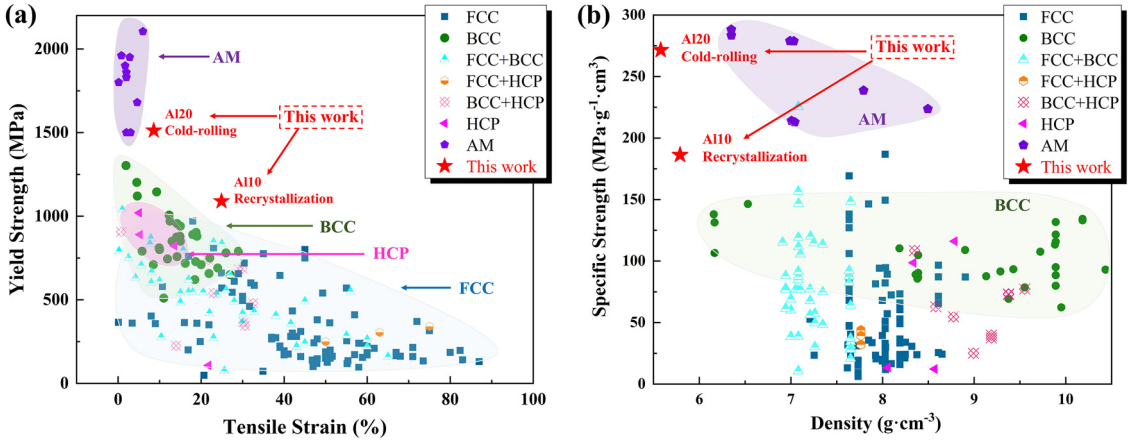

Fig. 7. Comparison of the current BCC–HEAs with existing HEAs and amorphous alloys. (a) Maps of yield strength versus tensile strain of HEAs and amorphous alloys reported previously at room temperature (Abbreviation: Yield strength (YS), Tensile strength (TS), Amorphous alloy (AM)). (b) Maps of specific strength versus density of HEAs and amorphous alloys reported previously at room temperature.

For the recrystallization Al10 alloy, short-rod dislocation and nanoprecipitates are the key factors, and the flexible interactions between dislocations and nanoprecipitates help to achieving effective strain-hardening ability.

4.4. Comparison of the mechanical properties

To demonstrate the performance advantage of BCC–HEAs in such a design concept, a comparison of tensile properties is conducted in the Fig. 7. Here, the intriguing HEAs are classified into six types, including FCC structure, BCC structure, hexagonal-close-packed (HCP) structure, and dual-phase structures between each other. Overall, the FCC–HEAs generally show excellent ductility but low yield strengths, while BCC–HEAs exhibit high yield strengths but poor ductility. The HCP-HEAs and dual-phase alloys occupy the middle region. Amorphous alloys generally have high strengths but fail to undergo tensile deformation. The data of the tensile properties and theoretical density of reported HEAs and amorphous alloys are acquired from Supplementary Table 1.

Fig. 7(a) shows the yield strengths and strains of current BCC–HEAs compared with those of reported HEAs and amorphous alloys. Remarkably, the cold-rolling $(Zr_{0.5}Ti_{0.35}Nb_{0.15})_{80}Al_{20}$ alloy exhibits extremely high strength comparable to the amorphous alloys, together with pretty good tensile ductility. This is a record-high strength known in BCC–HEAs. The recrystallization $(Zr_{0.5}Ti_{0.35}Nb_{0.15})_{90}Al_{10}$ alloy has significant advantages, including high strength and an excellent strength−ductility balance. It is worth noting that the tensile strain of ~25% in recrystallization Al10 alloy is almost the limit value over existing BCC–HEAs. Hence, the current BCC–HEAs show great potentials to fill the gap between the amorphous alloys and ductile BCC–HEAs, in the terms of both strength and toughness. We also compare the specific strength and density of current BCC–HEAs with those of reported HEAs in Fig. 7(b). The density of current $(Zr_{0.5}Ti_{0.35}Nb_{0.15})_{100-x}Al_x$ alloys is lower than that of most reported HEAs and amorphous alloys. Obviously, the developed BCC–HEAs occupy an unexplored space, where is both light and strong. The $(Zr_{0.5}Ti_{0.35}Nb_{0.15})_{100-x}Al_x$ alloys exhibit significant advantages over existing bulk HEAs in terms of specific strength, showing the enormous potential for advanced structural applications.

5. Conclusion

In summary, the $(Zr_{0.5}Ti_{0.35}Nb_{0.15})_{100-x}Al_x$ BCC–HEAs show ultra-high strength together and good tensile ductility, which can be developed as a potential low-density structural material. We demonstrate that the semi-coherent nanoprecipitates strengthening and flexible dislocation motion are the key factors to achieving this remarkable breakthrough. To overcome the weak strain hardening ability and further obtain outstanding mechanical properties, high-density dislocation cells and dense short-rod dislocations are designed via controlled thermo-mechanical treatments, which significantly improves the dislocation mobility and homogenizes dislocation microstructure. At the same time, semi-coherent nanoprecipitates also play a positive role on excellent comprehensive mechanical properties. The current results do not only provide a general method for developing BCC–HEAs with excellent comprehensive mechanical properties, but also prove the feasibility of obtaining effective strain-hardening capability. We expect that this design philosophy has significant implications in developing promising ultra-strong and ductile BCC–HEAs superior to existing commercial alloys.

Declaration of Competing Interest

The authors declare that they have no known competing financial interests or personal relationships that could have appeared to influence the work reported in this wrok.

Acknowledgements

Y. Z. acknowledges supports from (1) National Natural Science Foundation of China (NSFC, Granted Nos. 51671020); (2) Guangdong Basic and Applied Basic Research Foundation (No. 2019B1515120020); and (3) Creative Research Groups of China (No. 51921001). P. K. L. acknowledges supports from (1) the U.S. Army Office Project (W911NF-13-1-0438 and W911NF-19-2-0049) and program managers, Drs. Michael P. Bakas, David M. Stepp, and S. Mathaudhu; and (2) the National Science Foundation (Nos. DMR-1611180 and 1809640) and program directors, Drs. Judith Yang, Gary Shiflet, and Diana Farkas. We thank Dr. Y. D. W for reviewing and commenting on this paper.

Supplementary materials

Supplementary material associated with this article can be found, in the online version, at doi:10.1016/j.jmst.2021.08.034.

References

[1] E.P. George, D. Raabe, R.O. Ritchie, Nat. Rev. Mater. 4 (2019) 515–534.
[2] J.W. Yeh, S.K. Chen, S.J. Lin, J.Y. Gan, T.S. Chin, T.T. Shun, C.H. Tsau, S.Y. Chang, Adv. Eng. Mater. 6 (2004) 299–303.
[3] Y. Zhang, T.T. Zuo, Z. Tang, M.C. Gao, K.A. Dahmen, P.K. Liaw, Z.P. Lu, Prog. Mater. Sci. 61 (2014) 1–93.
[4] Q.Q. Ding, X.Q. Fu, D.K. Chen, H.B. Bei, B. Gludovatz, J.X. Li, Z. Zhang, E.P. George, Q. Yu, T. Zhu, R.O. Ritchie, Mater. Today 25 (2019) 21–27.
[5] G. Laplanche, A. Kostka, C. Reinhart, J. Hunfeld, G. Eggeler, E.P. George, Acta Mater 128 (2017) 292–303.
[6] P.J. Shi, Y.B. Zhong, Y. Li, W.L. Ren, T.X. Zheng, Z. Shen, B. Yang, J.C. Peng, P.F. Hu, Y. Zhang, P.K. Liaw, Y.T. Zhu, Mater. Today 41 (2020) 62–71.
[7] Y.J. Liang, L.J. Wang, Y.R. Wen, B.Y. Cheng, Q.L. Wu, T.Q. Cao, Q. Xiao, Y.F. Xue, G. Sha, Y.D. Wang, Y. Ren, X.Y. Li, L. Wang, F.C. Wang, H.N. Cai, Nat. Commun. 9 (2018) 4063–4070.
[8] S.L. Wei, S.J. Kim, J.Y. Kang, Y. Zhang, Y.J. Zhang, T. Furuhara, E.S. Park, C.C. Tasan, Nat. Mater. 19 (2020) 1175–1181.
[9] D.X. Qiao, H. Jiang, W.N. Jiao, Y.P. Lu, Z.Q. Cao, T.J. Li, Acta Metall. Sin-Engl. 32 (2019) 3–9.
[10] W.R. Zhang, P.K. Liaw, Y. Zhang, Entropy 20 (2018) 951–971.
[11] L. Wang, C. Fu, Y.D. Wu, R.G. Li, Y.D. Wang, X.D. Hui, Mater. Sci. Eng. A 748 (2019) 441–452.
[12] S.P. Wang, J. Xu, Mater. Sci. Eng. C 73 (2017) 80–89.
[13] H.L. Huang, Y. Wu, J.Y. He, H. Wang, X.J. Liu, K. An, W. Wu, Z.P. Lu, Adv. Mater. 29 (2017) 1701678.
[14] Y. Zou, S. Maiti, W. Steurer, R. Spolenak, Acta Mater 65 (2014) 85–97.
[15] S. Sheikh, S. Shafeie, Q. Hu, J. Ahlström, C. Persson, J. Veselý, J. Zýka, U. Klement, S. Guo, J. Appl. Phys. 120 (2016) 164902.
[16] S.S. Sohn, A.K. Da Silva, Y. Ikeda, F. Koermann, W. Lu, W.S. Choi, B. Gault, D. Ponge, J. Neugebauer, D. Raabe, Adv. Mater. 31 (2019) 1807142.
[17] L. Lilensten, J.P. Couzinié, L. Perrière, A. Hocini, C. Keller, G. Dirras, I. Guillot, Acta Mater 142 (2018) 131–141.
[18] O.N. Senkov, J.M. Scott, S.V. Senkova, D.B. Miracle, C.F. Woodward, J. Alloys Compd. 509 (2011) 6043–6048.
[19] Z. Li, K.G. Pradeep, Y. Deng, D. Raabe, C.C. Tasan, Nature 534 (2016) 227–230.
[20] J.Y. He, H. Wang, H.L. Huang, X.D. Xu, Z.P. Lu, Acta Mater 102 (2016) 187–196.
[21] B. Gwalani, D. Choudhuri, V. Soni, Y. Ren, M. Styles, J.Y. Hwang, S.J. Nam, H. Ryu, S.H. Hong, R. Banerjee, Acta Mater 129 (2017) 170–182.
[22] S.H. Jiang, H. Wang, Y. Wu, X. Liu, H. Chen, M. Yao, B. Gault, D. Ponge, D. Raabe, A. Hirata, M. Chen, Y. Wang, Z.P. Lu, Nature 544 (2017) 460–464.
[23] I.S. Wani, T. Bhattacharjee, S. Sheikh, Y.P. Lu, S. Chatterjee, P.P. Bhattacharjee, S. Guo, N. Tsuji, IOP Conf. Ser.: Mater. Sci. Eng. 194 (2017) 012018.
[24] Z. Fu, B.E. Macdonald, Z. Li, Z. Jiang, W. Chen, Y. Zhou, E.J. Lavernia, Mater. Res. Lett. 6 (2018) 634–640.
[25] Z.Z. Li, S.T. Zhao, R.O. Ritchie, M.A. Meyers, Prog. Mater. Sci. 102 (2019) 296–345.
[26] T. Yang, Y.L. Zhao, Y. Tong, Z.B. Jiao, J. Wei, J.X. Cai, X.D. Han, D. Chen, A. Hu, J.J. Kai, Science 362 (2018) 933–937.
[27] J.Ph. Couzinié, L. Lilensten, Y. Champion, G. Dirras, L. Perrière, I. Guillot, Mater. Sci. Eng. A 645 (2015) 255–263.
[28] J.L. Chaussidon, M. Fivel, D. Rodney, Acta Mater 54 (2006) 3407–3416.
[29] K. Srivastava, D. Weygand, D. Caillard, P. Gumbsch, Nat. Commun. 11 (2020) 5098.
[30] S.I. Hong, C. Laird, Acta Mater 38 (1990) 1581–1594.
[31] J.P. Hirth, J. Lothe, Theory of Dislocations, McGraw-Hill Book Company, New York, 1972.
[32] S.I. Rao, C. Varvenne, C. Woodward, T.A. Parthasarathy, D. Miracle, O.N. Senkov, W.A. Curtin, Acta Mater 134 (2017) 311–320.
[33] B. Chen, S. Li, H. Zong, X. Ding, E. Ma, Proc. Natl. Acad. Sci. U.S.A. 117 (2020) 201919136.
[34] F.L. Wang, G.H. Balbus, S.Z. Xu, Y.Q. Su, J.H. Shin, P.F. Rottmann, K.E. Knipling, J.C. Stinville, L.H. Mills, O.N. Senkov, I.J. Beyerlein, T.M. Pollock, D.S. Gianola, Science 370 (2020) 95–101.
[35] Z.F. Lei, X.J. Liu, Y. Wu, H. Wang, S.H. Jiang, S.D. Wang, X.D. Hui, Y.D. Wu, B. Gault, P. Kontis, D. Raabe, L. Gu, Q.H. Zhang, H.W. Chen, H.T. Wang, J.B. Liu, K. An, Q.S. Zeng, T.G. Nieh, Z.P. Lu, Nature 563 (2018) 546–550.
[36] X.H. Yan, J. Ma, Y. Zhang, Sci. China Phys. Mech. 62 (2019) 996111.
[37] X.H. Yan, Y. Zhang, Scr. Mater. 178 (2020) 329–333.
[38] A. Takeuchi, A. Inoue, Mater. Trans. 46 (2005) 2817–2829.
[39] S.B. Wang, M.X. Wu, D. Shu, G.L. Zhu, D.H. Wang, B.D. Sun, Acta Mater 201 (2020) 517–527.
[40] D. Caillard, Acta Mater 61 (2013) 2808–2827.
[41] E. Nembach, Particle Strengthening of Metals and Alloys, Wiley-VCH, New York, 1997.